Exploring the influence of flexibility on rotor performance in turbulent flow environments

Marwa Fakhfekh, Wael Ben Amira, Malek Abid, Aref Maalej

Exploring the Influence of Flexibility on Rotor Performance in Turbulent Flow Environments

Fakhfekh Marwa[1], Ben Amira Wael[1], Abid Malek[2*] and Maalej Aref[1,3]

[1]Laboratory of Electromechanical Systems, National Engineering School of Sfax - University of Sfax, Soukra km 3.5, Sfax, 3038, State, Tunisia.

[2*]Aix-Marseille Université, Institut de Recherche sur les Phénomènes Hors Equilibre, UMR 7342, CNRS, Centrale Méditerranée, 49 rue Joliot Curie - BP 146 Technopôle de Château Gombert, Marseille, 13384, France.

[3]Department of Electrical and Electronic Engineering Science, University of Johannesburg, Johannesburg 2006, South Africa.

*Corresponding author(s). E-mail(s): malek.abid@univ-amu.fr;
Contributing authors: marwa.fakhfekh@enis.tn; benamira.wael@gmail.com; aref.maalej@enis.tn;

Abstract

Flexibility plays a crucial role in the design and performance of modern rotors. Its impact on rotor performance and its ability to adapt to external flow disturbances are well-established. In this study, we employ numerical simulations to explore the behavior of a flexible rotor submerged in a turbulent flow, aiming to forecast the influence of its flexibility on performance metrics. The rotational motion of the rotor and the forces imposed by the flow induce deformations in the blades, including bending and twisting. These deformations not only disrupt the flow patterns (vortices) in the turbulent wake but also modify the aerodynamic profiles, thereby affecting essential performance aspects such as thrust, drag, and lift. Our objective is to uncover the relationships between blade deformations, rotation frequencies, and rotor performance in a turbulent flow with a Reynolds number, $Re = O(10^4)$, and for a tip speed ratio in the range $[0, 18]$. We demonstrate that the mean blade bending angle can be effectively expressed using a modified Cauchy number, revealing a scaling law. We also examined how the aerodynamic performance of the rotor blade is affected by variations in the tip speed ratio, either amplifying or reducing it. Through this research, we advance our understanding of the interplay between rotor flexibility, deformation, and performance, contributing to the optimization of rotor design and operational efficiency.

Keywords: Numerical simulations, flexible rotor blade, rotor performances, blade deformation, rotation frequency, pitch angle

1 Introduction

Rotors find extensive applications in both man-made propulsion systems and energy conversion and collection devices. Traditionally, these rotors have been rigidly designed to avert potentially destructive deformations. For instance, in the case of wind turbines, it is essential to ensure that the blades do not bend and collide with the hub, especially in high winds. However, the use of composite materials in various modern design applications, coupled with the increasing global energy demand, has led to a remarkable upscaling of wind turbines, making these deformations increasingly unavoidable.

The design of rotor blades plays a pivotal role in the conversion of flow energy into mechanical energy. In general, the rotor design process is centered on enhancing their performance, which, in turn, hinges on how the rotors are utilized. Some rotor designs aim to increase drag and diminish lift, while others strive to enhance lift over drag.

For example, the performance of turbine blades is profoundly influenced by rotational forces [1], encompassing lift and drag [2]. The lift force acts perpendicularly to the fluid flow, propelling the rotation, while the drag force is in the direction of flow. Efficiency is optimized by maximizing lift and minimizing drag [3], which typically occur concurrently. The drag coefficient can be used to estimate the frequency of profile vortex shedding [4].

Improving the performance of these rotors primarily involves the optimization of key aerodynamic parameters, notably the airfoil shape and blade geometry [5]. The growing preference for flexible blades is underpinned by their superior wind-capturing ability, stress reduction on the turbine, and their positive impact on overall performance and longevity [5]. Consequently, wind turbine manufacturers are placing increased emphasis on the development of more flexible blade designs, owing to their inherent advantages, including reduced weight, enhanced transportability, and the potential to curtail both costs and installation time.

In the contemporary rotor design landscape, flexibility must now be regarded as a paramount consideration [6, 7]. This paradigm shift extends beyond wind turbines, finding relevance in diverse applications such as helicopters and micro air vehicles. In these contexts, rotors outfitted with highly flexible blades are naturally integrated to enhance the safety of small drones [8, 9]. Moreover, flexible rotor systems are deployed in innovative configurations, such as the retractable designs exemplified by Sicard and Sirohi [10], where the blades can be wound into the hub.

The utilization of flexible materials in the design of rotors or moving bodies presents both advantages and drawbacks, as evidenced by numerous instances in the natural world. In a fluidic context, flexibility offers distinct advantages: for example, plants exhibit leaf curvature to mitigate wind-induced drag [11], while birds enhance wing-flapping efficiency through wing deformability [12]. Nevertheless, it is crucial to acknowledge that deformations can also influence flow stability [13].

In a broader context, nature provides a compelling demonstration of how flexibility augments an object's ability to adapt to variations in external conditions within fluid flows. A comprehensive examination of plant behavior in flowing environments [14–16] underscores their capacity to dynamically reconfigure in order to minimize their wind-exposed surface area. This proactive response not only reduces drag but also ensures their survival during extreme events.

Numerous studies have delved into the impact of flexibility in various contexts. For instance, Dai et al. [17] conducted research focusing on the assessment of structural flexibility and its influence on performance. Another relevant investigation is the one carried out by Gosselin et al. [11], which introduced an experimental setup designed to scrutinize the effects of flexibility and reconfiguration on drag reduction. A pivotal aspect of their work was the determination of the Voguel number, a parameter that plays a crucial role in the velocity exponent in the drag force expression. Specifically, in the case of rigid bodies, the drag force increases proportionally to the square of the flow velocity, whereas for flexible bodies, flexibility mitigates the rate of change of the drag force with respect to velocity. Consequently, the Voguel number moderates the velocity power coefficient. Additionally, Tayyaba et al. [18] utilized fluid-structure interaction methods in their research to investigate various aerodynamic parameters for flexible flaps situated within the flow.

For rotating structures, research has demonstrated the advantageous impact of flexible deformations on performance. In fact, Motley et al. [19] illustrated how leveraging the anisotropic characteristics of composite materials can enhance the efficiency of marine propellers through tailored flexibility adjustments. There exists an inherent correlation between the deformation of a rotating structure and the distribution of forces on a blade. Cognet et al. [20, 21] have established that, depending on the wind turbine's design and the wind distribution, it is feasible to identify elastic properties that augment the turbine's performance by expanding its operational range.

Numerous recent studies have proposed the integration of deformed wind turbine blades, with one noteworthy investigation conducted by Castillo [22]. Employing an experimental approach, Castillo examined the performance of a flexible wind turbine blade and its implications for load reduction.

In a similar vein, Eldemerdash and Leweke [23] conducted an experiment to delve into the fluid-structure

interaction of a flexible blade submerged in a water tank. Their objective was to assess the influence of hydrodynamic properties on blade elasticity and to elucidate how flexibility impacts the wake generated behind the blades.

Furthermore, Hörner et al. [24] conducted comprehensive experimental research on the fluid-structure interaction of Darrieus water turbines with highly flexible blades, uncovering a plethora of intriguing findings. Their primary objective was to ascertain the optimal blade flexibility, underpinned by an analysis of vibration frequency and tip speed ratio across varying stiffness levels, thereby validating the turbine's design for both rigid and flexible configurations.

In a similar vein, Gao et al. [25] undertook a combined experimental and numerical analysis of the aerodynamic performance of vertical axis wind turbines employing flexible drag-lift hybrid structures based on a symmetrical aerodynamic profile, NACA0018. Their findings demonstrated that the drag-lift hybrid design significantly enhances wind energy utilization compared to traditional lifting blades.

Additionally, Oukasso et al. [26] explored the optimal angle of attack for NACA0012 and NACA2412 airfoils to maximize lift and drag ratios, employing the Computational Fluid Dynamics method. Their research underscored the substantial impact of airfoil choice on turbine efficiency, with the NACA2412 airfoil outperforming the NACA0012 variant in terms of efficiency and maximum power output.

Eldemerdash and Leweke [23] conducted a recent investigation involving a rotor consisting of slender plastic blades immersed in water. Their research encompassed the measurement of the flow field surrounding these blades, as well as the assessment of deformations. The study's findings revealed that substantial bending is noticeable during forward motion and that large-amplitude oscillations occur during reverse motion. Although the study provides thrust estimations for specific parameters utilizing the flow field data, it's worth noting that no direct measurements were executed.

As mentioned earlier, research on flexible rotors, and aeroelasticity in general, often relies on experimental investigations. While numerical simulations can be employed to address such challenges, they offer advantages beyond optimizing blade performance, including the potential to save time and money by assessing blade functionality prior to fabrication.

In our prior research [27], we conducted a numerical analysis rooted in fluid-structure interaction to explore the aerodynamic behavior of a rotor with flexible blades submerged in water. This study involved characterizing blade deformations based on blade geometry and flow conditions. Our findings demonstrated that the blades exhibit downstream deformations with varying amplitudes contingent upon the rotation frequency. In specific configurations with certain pitch angles and rotation frequencies, the blades deform in the opposite direction. Furthermore, we presented and discussed the flow wake patterns trailing the blades and the occurrence of the vortex ring state.

In the present study, we develop a numerical investigation based on fluid-structure interaction to examine the impact of blade flexibility on rotor performance. We elucidate the performance exhibited by a one blade rotor, operating within a water environment, and delve into how this performance is altered by the blade deformation.

2 Numerical simulation of fluid-structure interaction problem

The investigation of aeroelastic behavior in rotors with flexible blades and the prediction of their performance necessitate a study and solution of the fluid-structure interaction problem. Such problems can be approached experimentally, mathematically, or through numerical methods. The simultaneous solution of both the structural and fluid equations, while adhering to coupling and interaction conditions, is paramount.

There are two primary methods for addressing the fluid-structure interaction problem: one-way fluid-structure interaction and two-way fluid-structure interaction. In this paper, we employ the two-way fluid-structure interaction method due to its superior accuracy, particularly in handling substantial structural deformations [28]. This method combines a fluid dynamics solver based on the finite volume method for solving fluid equations and a transient structural dynamics solver based on the finite element method to address the motion equations within the structural domain. The coupling between the two domains is facilitated through an interface coupling system, which sequentially transfers data from the fluid to the structure and vice versa, ensuring compliance with coupling conditions.

As a result of these interactions, the fluid domain is

updated whenever mesh interlocks occur due to structural deformation, and the structure undergoes deformation due to pressures present in the fluid domain. It is worth noting that simulating such a complex problem is time-intensive.

2.1 Governing equations:

To explore the intricacies of fluid-structure interaction (FSI), we employ the governing equations represented by the incompressible Navier-Stokes equations, for the fluid flow, coupled with the linear elastic equations, for the solid motion. The model equations are:

$$\rho_f \frac{\partial \mathbf{u}_f}{\partial t} + \rho_f(\mathbf{u}_f \cdot \bigtriangledown)\mathbf{u}_f = -\bigtriangledown p + \mu_f \bigtriangledown \cdot (\bigtriangledown \mathbf{u}_f) + F_v, \quad (1)$$

$$\bigtriangledown . \mathbf{u}_f = 0, \quad (2)$$

$$\rho_s \frac{\partial^2 \mathbf{x}_s}{\partial t^2} - \nabla \cdot \boldsymbol{\sigma}^{solid} = F_s. \quad (3)$$

In the context of these equations, where $\mathbf{u}_f$ represents the incompressible fluid velocity field, $\mathbf{x}_s$ corresponds to the displacement of the solid blade, t denotes time, p represents the pressure field , μ_f stands for the dynamic viscosity, F_v signifies the body force acting on the fluid (in this case, gravitational acceleration multiplied by ρ_f), and F_s characterizes the force per unit volume acting on the blade. The densities of the fluid and solid, ρ_f and ρ_s, respectively, are also accounted for.

The stress field within the fluid, denoted as σ^{fluid}, is described by the subsequent equation:

$$\boldsymbol{\sigma}^{fluid} = -pI + \mu_f \nabla \mathbf{u}_f. \quad (4)$$

Furthermore, the Hooke's law is used:

$$\boldsymbol{\sigma}^{solid} = 2\mu_s \boldsymbol{\epsilon} + \lambda_s tr(\boldsymbol{\epsilon})\mathbf{I}, \quad (5)$$

$$\mu_s = \frac{E}{2(1+\upsilon)}, \qquad \lambda_s = \frac{E\upsilon}{(1+\upsilon)(1-2\upsilon)} \quad (6)$$

where $\boldsymbol{\sigma}^{solid}$ is the stress field, $\boldsymbol{\epsilon}$ is the solid deformation, E is the Young's modulus, υ is the Poisson coefficient, $tr()$ is the trace and $\mathbf{I}$ is the identity tensor. The coupling equations are modeled by two conditions:

- a kinematic condition given by:

$$\mathbf{u}_f(x,t) = \frac{\partial \mathbf{x}_s}{\partial t}, \qquad \text{on the blade,} \quad (7)$$

- a dynamic condition represented by the following equation:

$$\mathbf{n}.\boldsymbol{\sigma}^{solid}_{interface} = \mathbf{n}.\boldsymbol{\sigma}^{fluid}_{interface}, \quad (8)$$

where $\mathbf{n}$ is the unit vector normal to the interface (i.e., the blade).

The kinematic condition entails an equating of the fluid and solid velocities, fostering a synchronized mesh movement for both domains. Consequently, during the mesh position updates, the solid displacement velocity is transferred to the fluid. In contrast, the dynamic condition aligns with the interaction of fluid forces exerted on the solid interface.

2.2 Computational Fluid Dynamics Model

The time-dependent fluid dynamics aspect of our fluid-structure interaction problem is developed using Ansys Fluent software. The transient fluid domain is discretized into a finite number of control volumes, following which the governing momentum conservation and general continuity equations are numerically resolved.

The computational fluid component is partitioned into two distinct regions: a stationary rectangular domain, representing the flow channel, featuring dimensions of 38 cm in width (2.16D, D being the rotor diameter), 52.8 cm in height (3D), and 176 cm in length (10D). Additionally, there is a cylindrical domain encompassing the rotor, blade, and hub, which undergoes rotation through a sliding mesh approach, exhibiting a diameter of 27 cm (1.53D) and a length of 50 cm (1.53D). This rotation simulates the motion of the turbine around its principal axis. The reference point (x, y, z) = (0, 0, 0) is established at the center of the turbine hub, as depicted in Figure 1. Rotor blade and hub's dimensions are depicted in Figure 2.

The Navier-Stokes equations are extended by incorporating the conventional $k-\varepsilon$ turbulence model. The rationale for selecting this turbulence model has been elucidated in our prior work [27]. In specifying the inlet boundary conditions for the channel, we set an inflow velocity of 0.18 m/s, with a turbulence intensity less than 1% based on reference

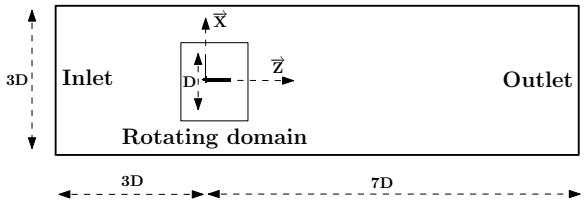

Fig. 1 Dimensions of fluid domains.

[23]. For the outlet, a pressure outlet boundary condition is imposed with a pressure value of 0 Pa. The channel walls and the CFD-coupled interface, comprising the hub, blade, and shaft, are treated as no-slip walls, indicating that the fluid adjacent to the wall assumes the same velocity as the wall itself.
The rotational behavior is defined by an angular velocity, $\omega = 2\pi f$, where f signifies the rotor's frequency.

2.3 Transient structure Model

The dynamic structural segment of our fluid-structure interaction problem is represented within the transient structure component system in ANSYS Workbench. This segment is primarily founded on Finite Element (FE) analysis techniques employed to address the elastic motion of the rotor blade. The geometric configuration of the rotor used in the CFD analysis has been seamlessly shared between the CFD and FE modules. The rotor has been endowed with angular velocity for z-axis rotation to account for the influence of centrifugal forces and align with the prescribed rotational speed within the CFD cylindrical domain. A displacement boundary condition at a specific distance is applied to the rotor, permitting rotation to manifest at any spatial location. To facilitate the exchange of data between the CFD and FE modules, the blade surfaces are treated as fluid-structure coupling interfaces. For comprehensive insights into the rotor's geometry and its aerodynamic attributes, please refer to Table 1 and Figure 2.

The blade is made of low-density polyethylene (LDPE), whose properties are shown in Table 2. The carbon material is assigned to the hub and the nylon to the shaft.

2.4 Coupled Fluid Structure Interaction Model

The coupling system was implemented in Ansys Workbench to facilitate the two-way connection between the fluid dynamics and structural analysis systems. To better understand the behavior of the structural domain in response to the fluid domain, information is exchanged between the structural solver and the fluid solver at the interface, forming the foundation of the fluid-structure interaction (FSI) model [29].

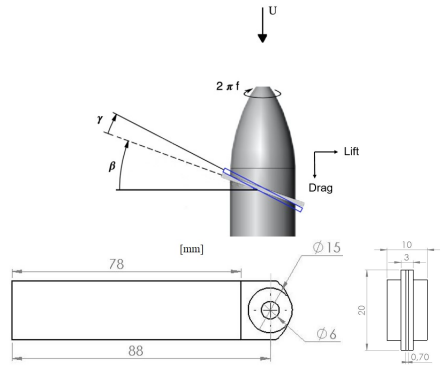

Fig. 2 Rotor, blade and hub's dimensions. Initially, there is no twist (or torsion) γ and β is the pitch angle. The frequency of the rotor is f and the uniform inlet (free stream) velocity is U_0.

Table 1 Blade and rotor parameters

parameter	value
Blade profile	Rectangular
Number of blades	1
Rotor Radius (R) [mm]	88
Blades Chord (C) [mm]	20
Blade thickness [mm]	0.7 (3.5 %C)
Shaft axis [mm]	15

Table 2 Blade material Property

Property	value
Density [Kg/m^3]	1070
Young's modulus [GPa]	3.5
Shear modulus [GPa]	1.7

2.5 Meshing

The meshing of the fluid domain was executed using Ansys Workbench. Multiple mesh configurations, encompassing both structured and unstructured meshes, were rigorously evaluated to ascertain the optimal mesh setup that would yield accurate results while maintaining computational efficiency. Tetrahedral cells were employed within the cylindrical and solid domains, while a hexahedral mesh was implemented for the remaining sections of the fluid domain. As a 3D dynamic mesh is incompatible with a structured mesh, as noted in prior studies [22, 28, 30], an unstructured mesh was adopted around the blade,

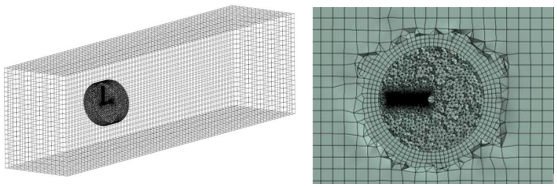

Fig. 3 Grid and sectional view of the computational domain.

specifically within the rotating domain. Conversely, a structured mesh was utilized in the stationary fluid domain, as illustrated in Figure 3. A well-balanced compromise was achieved, resulting in a total mesh size consisting of 454,188 nodes and 235,001 elements.

To accurately capture the blade's geometry, a finer mesh size of $0.001m$, corresponding to 20 elements along the chord, was employed at the fluid-structure coupling interfaces, particularly at the wall-CFD interface. For the two-way fluid-structure interaction, a dynamic mesh with remeshing, superposition, and smoothing options was implemented to facilitate seamless coupling and data exchange between the fluid dynamics solver and the transient structural solver.

Table 3 Structural Mesh sensibility : it is observed that when the element size decreases, there is a convergence of the drag force, F_D, towards a given value and the relative error decreases (relative error = $|F_D(\text{large mesh}) - F_D(\text{small mesh})|/F_D(\text{large mesh})$).

Chord/Element size	Drag Forces [N]	Relative Error(%)
7	0,147	–
10	0.1585	8
20	0.168	6
40	0.1639	2.5

The transient structural domain was meshed using an unstructured tetrahedral method, resulting in 13,795 elements and 27,707 nodes. The mesh size was specified as $0.001m$, corresponding 20 element along the chord at the blade level, consistent with the fluid domain, and $0.003m$ at the hub and shaft levels equivalent to 7 element along the chord, as illustrated in Figure 4.

The selection of this mesh size was made after careful consideration and was subsequently validated through simulations as part of a mesh sensitivity study conducted at the blade level. The results of this study can be found in Table 3.

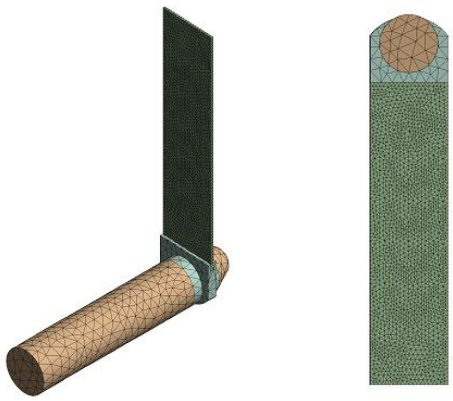

Fig. 4 Structure of the mesh.

3 Results and discussions

To establish an efficient numerical model for bidirectional data transfer, initial solution data was omitted for the first rotation [30, 31]. In this study, our primary focus is on the blade's behavior immediately following the transient phase, aimed at reducing simulation time. To achieve this, we selected a time frame of 3 seconds, equivalent to over 6 revolutions at a frequency of 2Hz. To ensure solution convergence and accurate data transfer at the coupling level, a time step of $1ms$ was utilized for frequencies below 5 Hz, with a smaller time step implemented for higher frequencies. Drawing upon the numerical results obtained from simulating the fluid-structure interaction problem, this paper delves into the impact of blade elasticity on rotor performance, encompassing factors like drag and lift. We examine two distinct scenarios: one involving a non-rotating structure and another with a rotating structure, allowing us to highlight the influence of rotation frequency on blade deformations and, subsequently, rotor performance.

In the following sections, we will examine various inlet velocities denoted by U, corresponding to Reynolds numbers, $Re = 2\pi fRc/\nu$, on the order of 10^4. Additionally, we will explore the tip speed ratio λ, defined as $\omega R/U$, which ranges from 0 to 18. Here, R represents the radius of the blade, ν signifies the kinematic viscosity of the surrounding fluid, and ω denotes the angular velocity of the rotating blade.

3.1 Non-rotating blade

In this section, we investigate the impact of input velocity on the drag force for a non-rotating blade in both rigid and flexible configurations, assuming a

pitch angle of $\beta = 0°$.

In the rigid case, the blade maintains a straight and unaltered shape, experiencing a drag force that changes in magnitude depending on the linear inlet velocity of the flow. (see Figure 5 and Figure 10). More precisely, the drag force is proportional to the square of the velocity, as illustrated in Figure 5 (a), where the drag coefficient is derived from the axial drag force F_D as depicted by the following equation:

$$C_D = \frac{F_D}{\frac{1}{2}\rho A U_i^2} \tag{9}$$

The rotor's swept area is denoted as A, ρ represents the fluid density, and U_i stands for a reference velocity.

The existing literature utilizes various reference velocities to define coefficients such as C_D, C_L (lift coefficient), and C_m (moment coefficient). These reference velocities can include the linear flow velocity, as suggested by [20, 32], or the addition of the angular rotational speed, as indicated by [33].

In this study, in order to account for the influence of rotation frequency, we determine the reference velocity as follows:

$$U_i = \sqrt{U^2 + (R\omega)^2} \tag{10}$$

The calculated drag coefficient is approximately $C_D \approx 1.22$, which aligns closely with the established value for a thin rectangular blade having an aspect ratio of $R/c = 4.4$ and at Reynolds numbers exceeding 1000 [34]. This alignment serves as a validation of both the mesh quality and the accuracy of turbulent flow and drag force computations in the current study.

The flexible blade, constructed from an elastic material, deforms in response to the pressure induced by the flow velocity. These deformations, relatively modest when compared to the rotating blade, amplify in accordance with the flow velocity (refer to the images in Figure 6 and the curves in Figure 7). It is worth mentioning that the tip displacements closely align with those derived for a cantilever beam uniformly charged with a linear distributed load, defined as $q = F_D/R$ (Figure 7b). In this case, the tip displacement can be expressed as $z_b = qR^4/(8EI)$. Furthermore, these deformations are directly related to the flow pressure, and their magnitudes follow a proportionality to the square of the velocity, as evidenced in Figure 8.

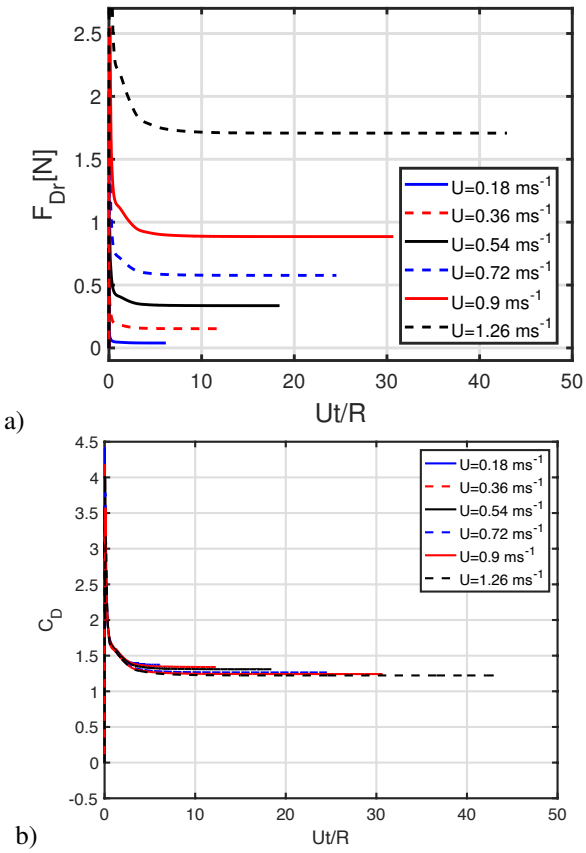

Fig. 5 a) Time evolution of drag forces for various inlet velocities in both rigid and non-rotating conditions. Nondimensional time, Ut/R, is used. b) Drag coefficients against nondimensional time. (For color, the reader is referred to the web version of this article).

In the case of a flexible blade, the drag force (F_{Df}) exhibits relatively modest values compared to the rigid case (F_{Dr}) (Figure 9). Specifically, at low inlet velocities, deformations are minimal, resulting in comparable values for F_{Df} and F_{Dr} ($F_{Df}/F_{Dr} \simeq 1$). As inlet velocities increase, deformations become more pronounced, leading to blade reconfiguration and a consequent reduction in drag. The maximum drag reduction observed is approximately 35%, occurring at the highest utilized inlet velocity (Figure 9 (b)). This moderation can be attributed to several factors. Firstly, the bending deformation of the blade reduces the projected surface area, resulting in a decrease in the drag force. Additionally, blade deformations introduce disturbances in the flow, which, in turn, can reduce the pressure on the blades and, consequently, the drag force.

To effectively demonstrate the impact of elasticity on drag force in the context of a stationary rotor, we

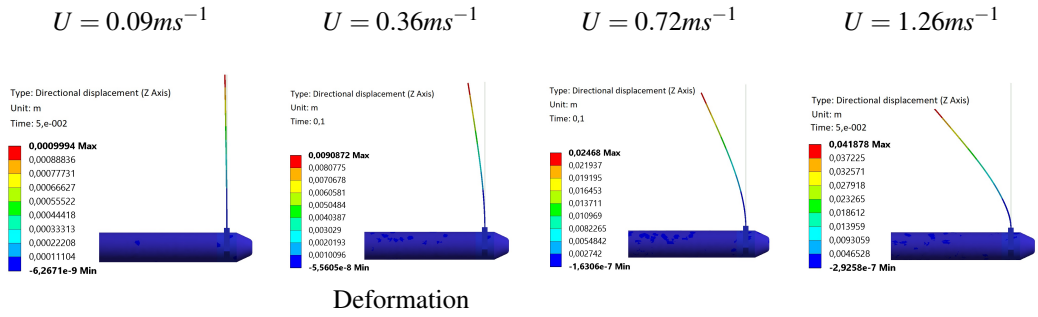

Fig. 6 Maximum flapwise displacement distribution of the blade with $\beta = 0°$, as function of the inlet velocity U. (For color, the reader is referred to the web version of this article).

depict in Figure 10 the drag force's evolution as a function of inlet velocity for both rigid and flexible blades.

From this figure, it is evident that the drag force's variation concerning inlet velocity follows a power law of order 2, indicating that the drag force is proportional to the square of velocity ($F_D \propto U^2$). This aligns with the theory describing drag force on a body in high Reynolds number flow. However, in the case of a flexible blade, the exponent of the power law is attenuated. This attenuation validates Vogel's law, which characterizes the variation of drag force with velocity for flexible bodies in flow. According to this law, the drag force follows a power law with an exponent of 2, moderated by a parameter $\mathscr{V}$ known as the Vogel number ($F_D \propto U^{2+\mathscr{V}}$) [11]. The Vogel number is material-dependent, and in our case, the exponent is 1.83, corresponding to a Vogel number of $\mathscr{V} = -0.17$.

To gain a deeper understanding of drag reduction in the flexible rotor through reconfiguration, we examine the reconfiguration number as proposed by Gosselin (2010) [35]. The reconfiguration number $\mathscr{R}$ emphasizes the effect of flexibility on the drag by comparing the drag of the flexible plate to that of a rigid one of same geometry. According to [35], the reconfiguration number should only be a function of the scaled Cauchy number, i.e., $\mathscr{R} = \mathscr{R}(\tilde{C}_y)$ where:

$$\mathscr{R} = \frac{F_D}{(1/2)\rho U^2 A_R C_D}, \tilde{C}_y = C_y C_D, C_y = \frac{1/2(\rho R^3)U^2}{(EI/R)}, \quad (11)$$

where, A_R is the blade area C_y is the Cauchy number and C_D is the drag coefficient (equation 9). For $\tilde{C}_y > 10$, $\mathscr{R} \propto \tilde{C}_y^{-\alpha}$ and $\mathscr{V} = -2\alpha$ with $\alpha > 0$ [35]. The reconfiguration numbers are presented in figure 10 (b). It is clear that for speeds up to 0.72 m/s ($\tilde{C}_y < 10$), the flexible blades exhibit drag values similar to the rigid blades ($\mathscr{R} \simeq 1$). These low drag values are a result of the blades experiencing minimal deformation at lower speeds. Beyond this threshold ($\tilde{C}_y > 10$, corresponding to $\mathscr{R}$<1), the influence of flexibility and blade deformation on drag becomes more pronounced, further diminishing the drag force. As flow velocity increases, the pressure on the blades rises, and blade deformation becomes more significant, leading to a reduction in the projected surface area in the flow and, consequently, a decrease in drag. We can say that the drag force decreases due to the reconfiguration effect. Note that at a velocity of $U = 0.18m/s$, the Cauchy number is sufficiently small for the asymptotics $\mathscr{R} \propto \tilde{C}_y^{-\alpha}$ to be applicable.

3.2 Rotating blade

In this section, we investigate the impact of rotation on rotor performance parameters. As per our prior studies [27], we have demonstrated that the blade undergoes deformation in the opposite direction beyond a specific rotation frequency. In the current study, our focus centers on the frequency range where the blade deforms downstream. To achieve this objective and facilitate subsequent analysis, we maintain the free-stream velocity constant at $U = 0.18m/s$ and consider a frequency range spanning from 0 to 6 Hz for performance evaluation, corresponding to $\lambda \in [0, 18]$.

Figure 11 presents the drag force ratio between the flexible and rigid cases. It illustrates the influence of rotational velocity on the drag force for both flexible and rigid blade configurations. Notably, flexible-blade rotors display more pronounced fluctuations in the drag force compared to the non-rotating scenario. This observation can be explained by the fact that, for the rotating case, deformations are more significant, thus creating disturbances in the flow and notably remarkable instabilities, which account for the more

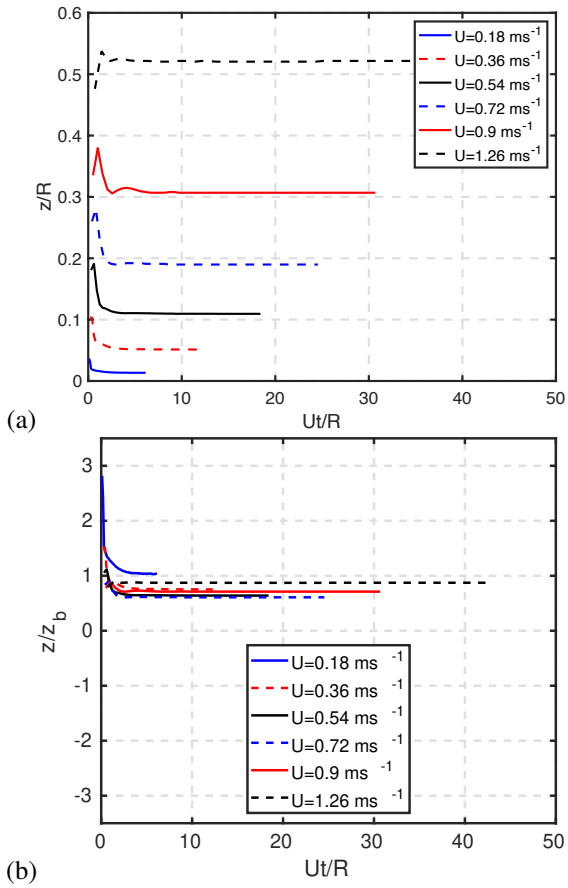

Fig. 7 Time evolution of the tip displacement, in the flexible non-rotating case, for different inlet velocities ($\beta = 0°$): a) normalized using the rotor radius; b) normalized using the tip displacement of a uniformly charged cantilever-beam with a linear distributed load, $q = F_D/R$, for which the tip displacement is $z_b = qR^4/(8EI)$. (For color, the reader is referred to the web version of this article).

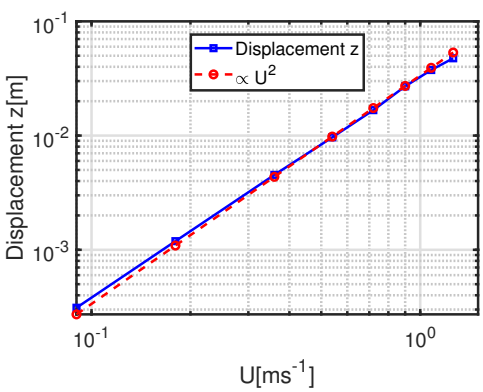

Fig. 8 Mean displacement plotted against inlet velocity (non-rotating case).

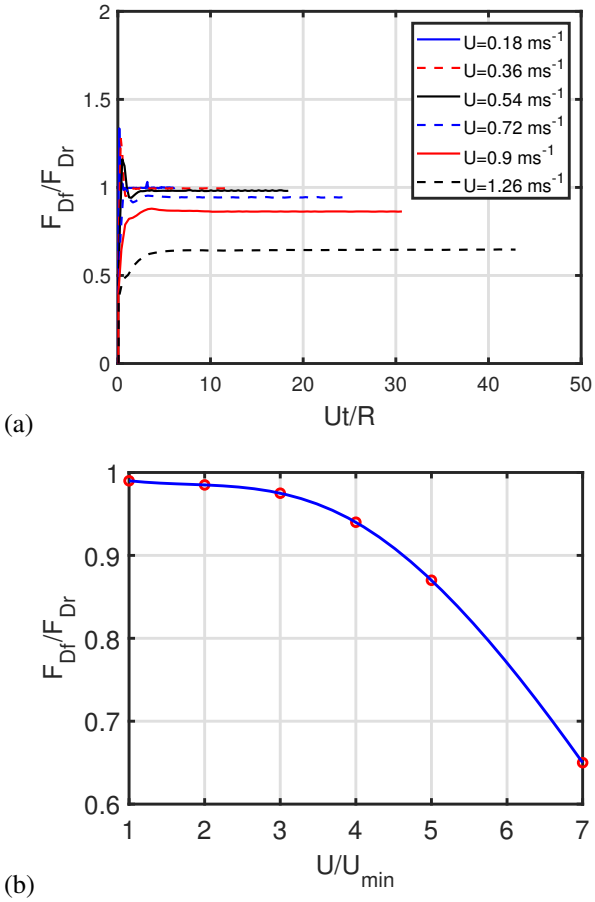

Fig. 9 (a) Drag force versus time for various inlet velocities in the flexible non-rotating blade scenario, denoted as F_{Df}, normalized by the drag force observed in the rigid non-rotating case, represented as F_{Dr}. (b) The ratio F_{Df}/F_{Dr} plotted against the inlet velocity post the transient phase. Inlet velocity is normalized using its minimum value utilized in this study, denoted as U_{min}. The solid line is the polynomial F_{Df}/F_{Dr}=$a_4(U/U_{min})^4 + a_3(U/U_{min})^3 + a_2(U/U_{min})^2 + a_1(U/U_{min}) + a_0$, with $(a_4, a_3, a_2, a_1, a_0) = (0.00049332, -0.008408, 0.03578, -0.060982, 1.0231)$. The root-mean-square error of this polynomial fit is of the order of 10^{-5}. (For color, the reader is referred to the web version of this article.)

pronounced fluctuations in the drag force of the rotating blade. Figure 11 further illustrates that a critical tip speed ratio, λ, exists. Beyond this threshold, the drag force exerted by the flexible blade surpasses that of its rigid counterpart. Indeed, As the tip speed ratio increases, the flexible blade deforms due to centrifugal and aerodynamic forces. The flexible blade undergoes oscillations which can increase the drag due to unsteady aerodynamic effects and periodic changes in angle of attack. Furthermore, the flexible blade might experience dynamic stall at higher λ, where the flow separates from the blade surface, causing a significant

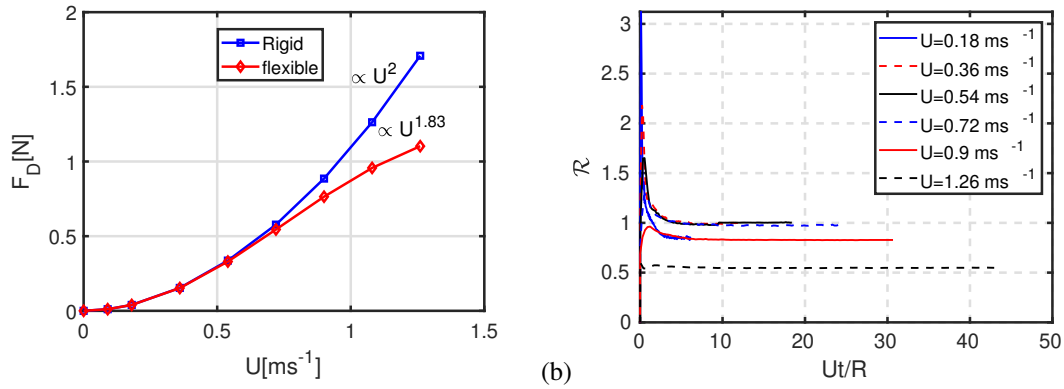

Fig. 10 (a) Variation of the drag force as a function of inflow velocity for the flexible and rigid cases (non-rotating case). (b) The reconfiguration number against nondimensional time. (For color, the reader is referred to the web version of this article).

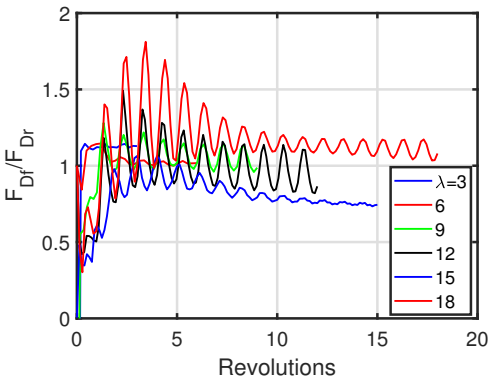

Fig. 11 The evolution of the drag force of the flexible rotor, F_{Df}, normalized against its rigid counterpart, F_{Dr}, for various tip speed ratios (or frequencies). (For color, the reader is referred to the web version of this article).

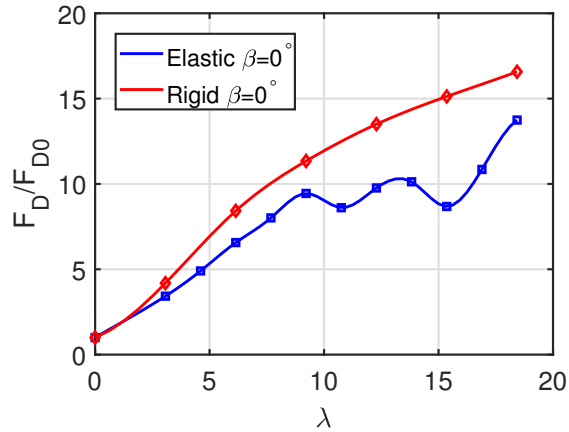

Fig. 12 Evolution of the drag force against the tip speed ratio for both the flexible and rigid cases. The forces are normalized relative to the force value at $\lambda = 0$, denoted as F_{D0}, $U = 0.18m/s$ and $\beta = 0°$. (For color, the reader is referred to the web version of this article).

increase in drag. This is more pronounced in flexible blades due to their tendency to bend and change their angle of attack. Note that flexible blades can induce greater vortices at their tips due to changes in shape and twist along the span, increasing induced drag. These tip vortices are more pronounced at higher tip speed ratios when the blade flexibility becomes significant. Nevertheless, it should be noted that, overall, the mean values of these two forces exhibit a tendency to become equal, at least for the range of tip speed ratios $0 \leq \lambda \leq 18$, studied here.

To demonstrate the influence of rotation frequencies on drag force, Figure 12 depicts the variation of drag force with the tip speed ratio (λ) for both rigid and flexible blade cases, with an inlet flow velocity of $U = 0.18$ m/s. These curves vividly illustrate that, in the rigid case, drag force increases continuously with rotation frequency, and consequently with the tip speed ratio. However, in the flexible case, the evolution of drag force with rotation frequency exhibits a more irregular pattern, which is primarily governed by blade deformation.

As the blade flexes, the projected surface area relative to the flow diminishes, thus moderating the drag force. In our earlier work [27], we elucidated that the bending deformation of the blade flexion for this configuration increases up to a frequency of 5 Hz; beyond this frequency, deformation amplitude commences to decrease. This phenomenon accounts for the inflection point in the drag force curve around $f = 5$ Hz ($\lambda \simeq 15$). This is confirmed in figure 13b. The deformation results are well validated by comparisons with Eldemerdash and Leweke's experimental findings [23], and these comparisions are done in our previous work

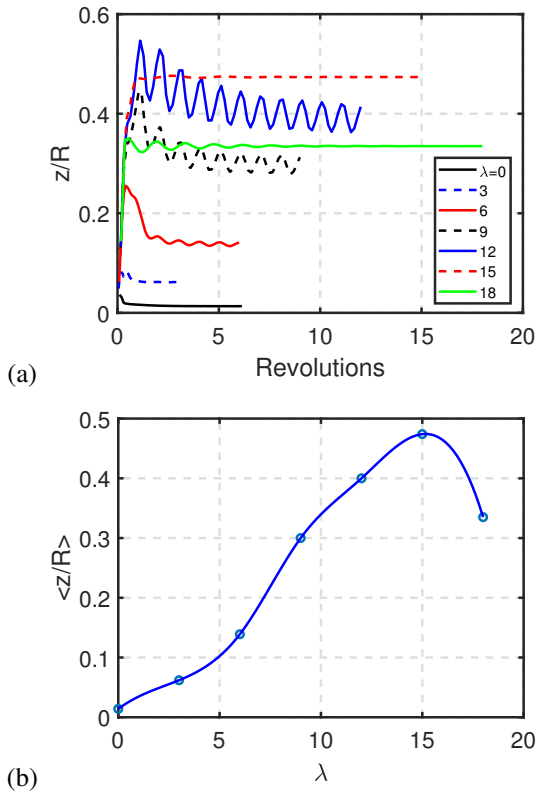

Fig. 13 (a) Evolution of the tip displacement (normalized by the rotor radius) for different tip speed ratios $\lambda = \omega R/U$: the flexible and rotating case. Note that for $\lambda = 0$, U/R is used for time normalisation instead of ω. (b) Evolution of the corresponding mean tip displacement against the tip speed ratio. (For color, the reader is referred to the web version of this article).

[27]. Figure 12 also highlights that with a sixfold increase in λ (with respect to its value at $\lambda = 3$), drag forces experience an approximate fourfold amplification for both flexible and rigid cases. Consequently, this amplification cannot be solely attributed to energetic considerations since the drag amplification is not equal to the square of that of λ.

The impact of rotation on tip displacement is illustrated in Figure 13 for various tip speed ratios λ. The displacement comprises two distinct components: a mean value and low-amplitude oscillations. As depicted in Figure 13a, the oscillations pulsate at the rotor's angular speeds ω. The mean tip displacement is shown in Figure 13b. It exhibits an increase with the tip speed ratio, reaching a peak at approximately half the blade radius for $\lambda = 15$, followed by a subsequent decrease. In comparison to the non-rotating scenario ($\lambda = 0$), the presence of rotation can amplify the displacement by a factor of up to 50. The maximum oscillations' small amplitudes are approximately 6/100 of the blade radius.

3.3 The impact of pitch and rotation on aerodynamic performance

The pitch angle has a significant effect on blade deformation and, consequently, on its aerodynamic performance. In this section, we will examine the impact of this angle on drag, lift, and moment. Figure 14 illustrates the variation of drag force with tip speed ratio for different pitch angle configurations, both for the rigid case (a) and the flexible case (b). In (c), the figure presents the ratio between drag forces in the flexible (F_{Df}) and rigid (F_{Dr}) cases. For a given tip speed ratio, in the rigid case, drag decreases as the pitch angle increases, which is attributed to the blade's orientation relative to the flow. The same behavior is observed with the flexible blade, meaning that drag reduces with an increase in the pitch angle, for the considered rotor blade. For a constant pitch angle, the drag force may either exhibit a monotonically increasing relationship with the tip speed ratio or not, depending on the pitch value. In cases where it is not monotonic, the drag force attains a maximum before decreasing, particularly at the highest pitch. In instances where the blade is flexible, an inflection point is observed in the absence of pitch, indicating a significant tip displacement. Figure 14 also highlights that with a sixfold increase in λ (with respect to its value at $\lambda = 3$), drag forces experience, at most, an approximate fourfold amplification for both flexible and rigid cases, even when the pitch is varied. In Figure 14 (c), it is evident that, for a specific pitch, the drag of the flexible blade may be either higher or lower than that of its rigid counterpart, contingent upon the tip speed ratio. Notably, at the maximum pitch, the drag of the flexible blade undergoes a maximum reduction by a factor of approximately three for the highest tip speed ratio, in comparison to its rigid counterpart.

To conduct a more comprehensive comparison of the drag generated by different rotor pitches, we introduce the normalized drag coefficient C_D, as depicted in equation 9.

The variation of the drag coefficient versus the tip speed ratio, as depicted in Figure 15, demonstrates notable similarities across different pitch angle configurations and for both flexible and rigid rotor cases. The drag coefficient exhibits a consistently decreasing

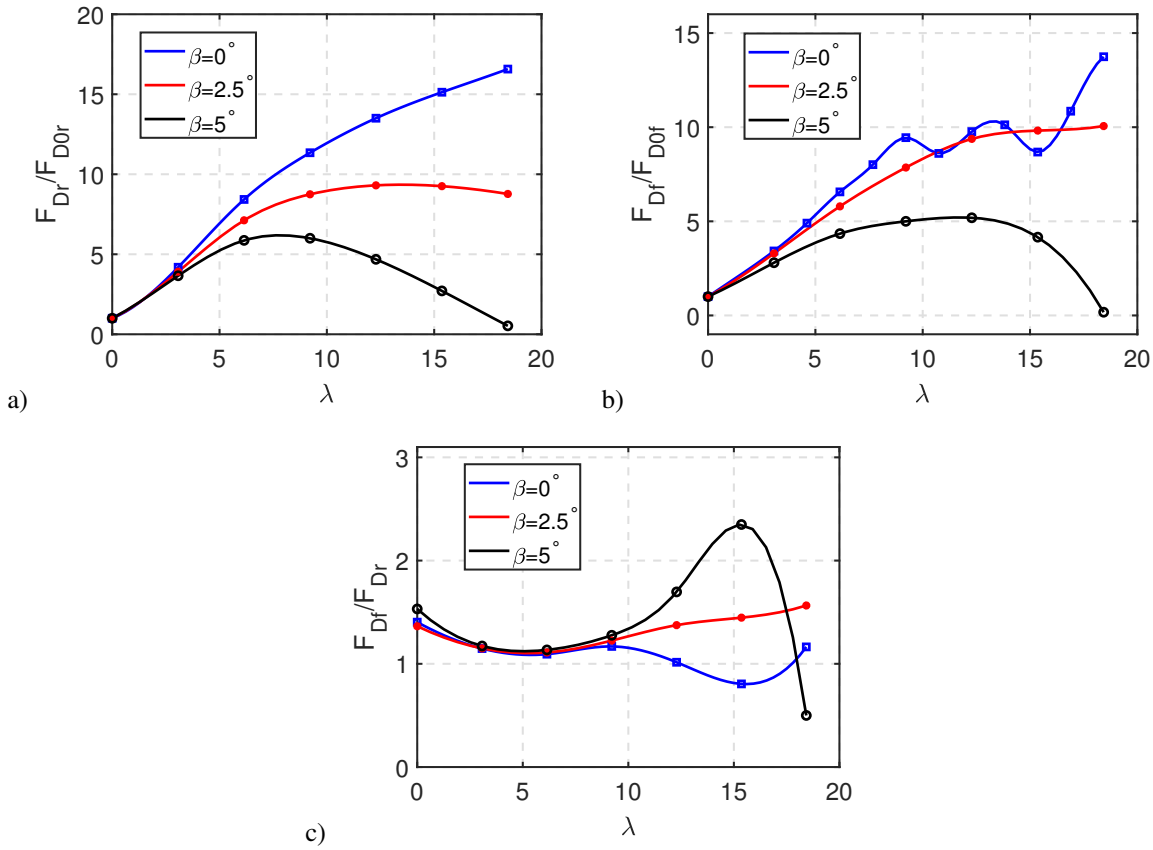

Fig. 14 Evolution of drag force against the tip speed ratio for both rigid (a) and flexible (b) cases, featuring various pitch angles. In (a) and (b), the forces are normalized with respect to the force value at $\lambda = 0$, identified as F_{D0r} and F_{D0f} for the rigid and flexible cases, respectively. In (c), the figure presents the ratio between drag forces in the flexible (F_{Df}) and rigid (F_{Dr}) cases. (For color, the reader is referred to the web version of this article).

trend as a function of the tip speed ratio, irrespective of the pitch angle. When the pitch angle is elevated, for both flexible and rigid scenarios, the drag coefficient (C_D) experiences a reduction, holding the tip speed ratio constant.

The examination of aerodynamic performance extends beyond the scope of drag force alone, encompassing lift force and moment as well. As with the drag coefficient, the lift coefficient C_L is determined by the following equation:

$$C_L = \frac{F_L}{\frac{1}{2}\rho A U_i^2} \tag{12}$$

Figure 16 presents the dynamic changes in lift coefficient over time at various rotation frequencies, offering a comparison between the rigid and flexible cases (with a pitch angle of $\beta = 0^\circ$ and $U = 0.18m/s$). In the rigid case, the oscillations in lift coefficient maintain a consistent pattern, whereas in the flexible case, these oscillations stabilize after a certain number of periods. This phenomenon is a direct result of the oscillations induced by blade deformation. Moreover, these oscillations share the same period as that of the rotating blade. After a transitory period, in the rigid scenario, the lift coefficient (C_L) oscillates within the range of 0.019 to -0.019. However, in the flexible case, the oscillations extend between 0.075 and -0.053, indicating that flexibility enhances the lift of the rotor blade under consideration and introduces a dissymmetry between positive and negative values of the lift.

To examine the impact of flexibility on lift, we conducted an analysis of lift force variation with respect to tip speed ratio for both rigid and flexible cases, using a rotor with a pitch angle of 0° as an illustrative example (Figure 17). The maximum value of the lift force, after the transitory period, is used. The findings

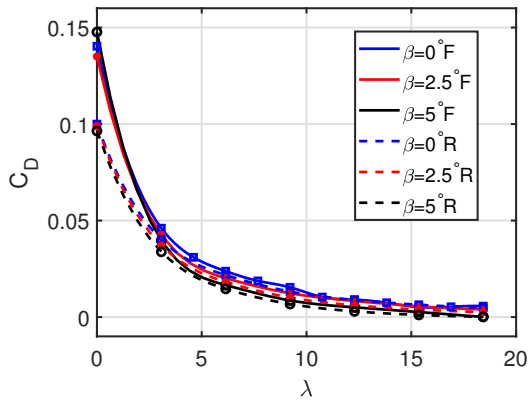

Fig. 15 The evolution of the drag coefficient as a function of tip speed ratio for different pitch angles, for both rigid (R) and flexible (F) cases. (For color, the reader is referred to the web version of this article).

unequivocally reveal that flexibility exerts a substantial influence on lift force.

In the case of a rigid structure, the lift force exhibits a monotonically increasing trend with the tip speed ratio. When the tip speed ratio is multiplied by a factor of six (with respect to its value at $\lambda = 3$), the lift force undergoes a fiftyfold increase, demonstrating an amplification exceeding a squared effect. Conversely, in the flexible case, the lift force, influenced by blade deformation, does not follow a monotonous pattern with respect to the tip speed ratio. It exhibits oscillations and may be lower than its rigid counterpart for a given tip speed ratio.

Figure 18 depicts the variation of lift force concerning the tip speed ratio for different pitch angles. In the context of rigid-blade rotors, the lift force behaves as a monotonically increasing function with respect to the tip speed ratio at various pitch angles. At a constant tip speed ratio, the lift force diminishes with an increase in the pitch angle. Consequently, when the tip speed ratio is multiplied by a factor of 6, the amplification of the lift force (with respect to its value at $\lambda = 3$) is 50 times for a pitch of 0°, 25 times for a pitch of 2.5°, and 19 times for a pitch of 5°.

In contrast, the behavior in the flexible case (Figure 18b) exhibits pitch-dependent characteristics regarding monotony. For $\beta = 0^\circ$, the lift force displays oscillations. However, for $\beta = 2.5^\circ$ and $\beta = 5^\circ$, the lift force regains monotonicity. This observation clearly highlights a significant influence of flexibility on the lift force, leading to a distinct profile. Nevertheless, the maximum amplification shows similar values compared to the rigid case.

The variation of this coefficient with respect to the tip speed ratio, for different configurations, is presented in Figure 19.

Figure 19 shows that for the rigid blade, the lift coefficient remains relatively low and stable across the entire range of tip speed ratios. There is a slight increase in C_L as the pitch angle increases from 0° to 5°, indicating that increasing the pitch angle has a modest effect on increasing the lift for the rigid blade. For the flexible blade, the lift coefficient shows much greater variability compared to the rigid blade. At $\beta = 0^\circ$, there are significant oscillations in C_L with peaks around λ = 5, 8, 13, and 15. This indicates that the flexible blade at zero pitch is experiencing periodic increases and decreases in lift, likely due to dynamic effects such as flutter or aerodynamic instabilities. As the pitch angle increases these oscillations become less pronounced, and the lift coefficient stabilizes somewhat, although it remains higher than for the corresponding rigid blade.

The recovered torque, or required torque, is a crucial parameter for characterizing rotor performance. Figure 20 displays the temporal variations of the $z-$moment, M, for different rotation frequencies in both the rigid and flexible cases. The moment is normalised using its value at $\lambda = 3$, denoted M_3. After a transitional period, the moments stabilize at constant values. These stable values indicate the magnification of the moment as λ increases. The magnification is of the order of 60 times when λ is multiplied by 6, observed in both rigid and flexible cases. To effectively depict the influence of flexibility on the moment, Figure 21 presents the variation of the normalised moment against the tip speed ratio for a pitch angle of $\beta = 0^\circ$. This figure highlights how flexibility leads to a decrease in the moment amplification for high values of λ.

This reduction can be ascribed to the enhanced adaptability of the blade facilitated by its flexibility, enabling it to better respond to the variable aerodynamic loads induced by the flow. As a consequence, this improved accommodation of forces leads to a decrease in the moment amplification generated by the blade. For low values of λ, the moment amplification is almost identical for both the flexible and rigid blade. Figure 22 showcases the progression of the moment concerning the tip speed ratio for various pitch angles, as demonstrated in both the rigid case (a) and the flexible case (b). In the rigid case,

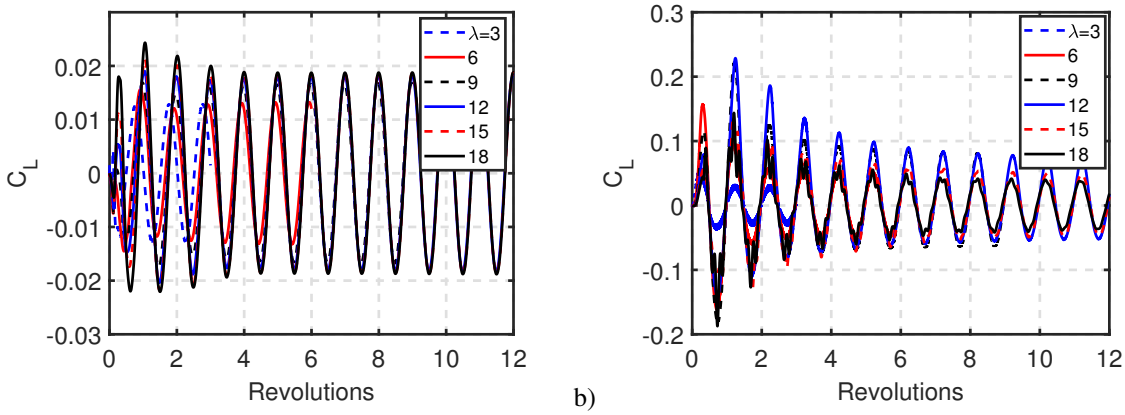

Fig. 16 Evolution of the lift coefficient, C_L, according to the number of rotor's revolutions for different tip speed ratios: a) rigid case, b) flexible case ($U = 0.18m/s$ and $\beta = 0°$). (For color, the reader is referred to the web version of this article).

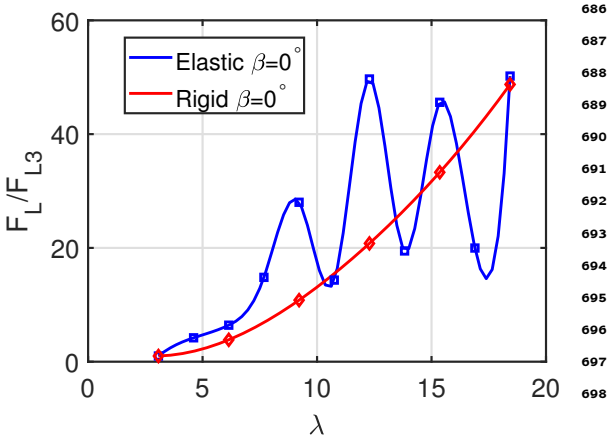

Fig. 17 Evolution of lift force with respect to tip speed ratio ($U = 0.18m/s$ and $\beta = 0°$). The lift force is normalized by its value at $\lambda = 3$, denoted as F_{L3}. (For color, the reader is referred to the web version of this article).

at a pitch angle of $\beta = 2.5°$, the moment amplification is heightened compared to the scenario without pitch as the tip speed ratio increases. However, this enhancement does not follow a monotonic trend, as the amplification diminishes with further increases in pitch ($\beta = 5°$). In the flexible case, the situation contrasts sharply, as the highest amplification occurs in the scenario without pitch, followed by the cases with $\beta = 2.5°$ and $\beta = 5°$, respectively.

The evolution of the moment coefficient is presented in Figure 23 (top), where the coefficient is defined by the following equation:

$$C_m = \frac{M}{\frac{1}{2}\rho A U_i^2 R} \tag{13}$$

Depending on the pitch value, the moment coefficient can be a monotonic or nonmonotonic function of λ. Further insights are gained by dividing it by its value at $\lambda = 3$, Figure 23 (bottom). It becomes evident that the amplification of C_m in the rigid case is consistently higher than in its flexible counterpart. Additionally, C_m may be amplified or reduced depending on the pitch. When λ is multiplied by a factor of 6, the maximum amplification does not exceed 2.5, for the considered blade and pitch values. It's worth noting that the reduction factor could reach 0.8 in the flexible case, and it is the higher $z-$moment reduction obtained for the considered blade configurations.

Another crucial parameter for studying rotor performance is the power coefficient. This fundamental coefficient provides an important insight into the overall efficiency of the rotor system. It is defined as the ratio between the power recovered by the rotor and the power available in the flow. The power coefficient is expressed by the following equation:

$$C_p = \frac{M.\omega}{\frac{1}{2}\rho A U_i^3} \tag{14}$$

where M is the rotor moment, ω is the rotation speed and U_i is the reference velocity defined by the relation 10. It is then easy to show that:

$$\frac{C_p}{C_{p3}} = \frac{C_m}{C_{m3}} \frac{\lambda}{3} \frac{\sqrt{10}}{\sqrt{1+\lambda^2}}. \tag{15}$$

Hence, an increase in the tip speed ratio could be inferred to affect the amplification of the power coefficient by examining those of the z-moment coefficient

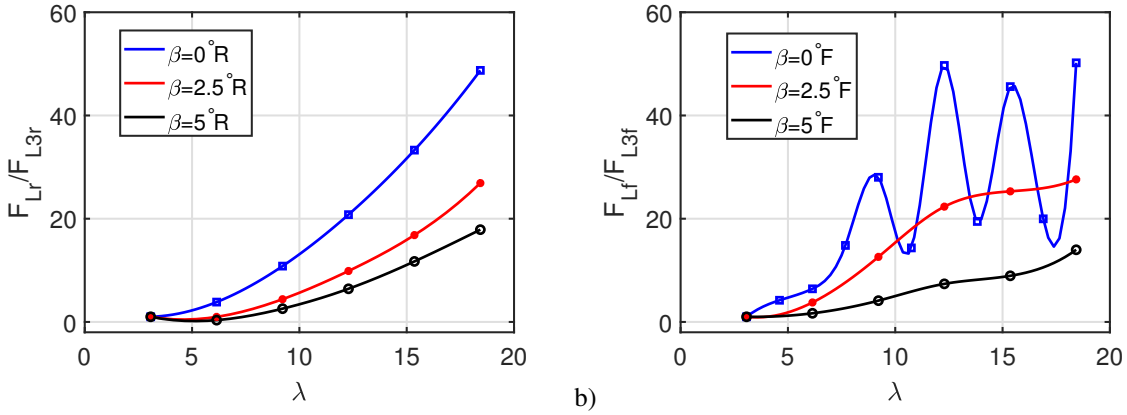

Fig. 18 Evolution of lift force as a function of tip speed ratio for different pitch angles and two distinct scenarios: a) the rigid case, and b) the flexible case. The forces are normalized using their respective values at $\lambda = 3$, identified as F_{L3r} and F_{L3f} for the rigid and flexible cases, respectively. (For color, the reader is referred to the web version of this article).

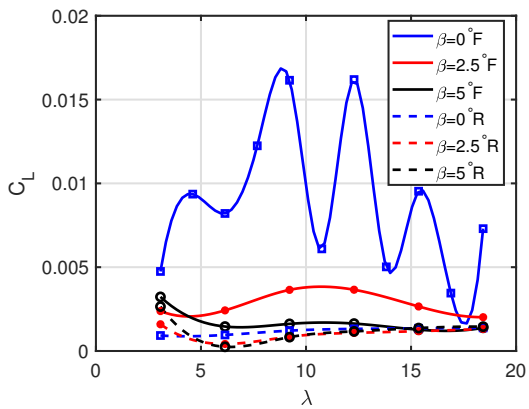

Fig. 19 Evolution of lift coefficient as a function of tip speed ratio for various pitch angles in both rigid and flexible cases. (For color, the reader is referred to the web version of this article).

(Figure 23).

4 A Scaling law for tip deformation

The forces acting on a blade from its environment encompass hydrodynamic forces (including lift and drag) as well as the centrifugal force. As evident from the discussed results, the lift force is notably smaller than the drag force (Data available, not shown) and plays a minor role in the flexing of the blade under consideration. In contrast, hydrodynamic forces significantly contribute to the bending deformation compared to the centrifugal force. Given these considerations and assumptions, we can safely neglect the influence of the centrifugal force and focus on the interaction between elasticity and fluid loading. Thus, the equation describing the bending of the blade during rotation is as follows [33]:

$$EI\frac{\partial^3\theta}{\partial s^3} = \frac{F_D}{R}\cos(\beta) = \frac{1}{2}\rho U_i^2\frac{A}{R}C_D\cos(\beta), \quad (16)$$

where ρ is the fluid density, U_i is the local apparent velocity (equation (10)). As previously stated, to characterize the interaction between elasticity and aerodynamic forces, we utilize the Cauchy (or elasto-hydrodynamical) number. This dimensionless number compares the intensity of hydrodynamic forces to the elastic modulus and is defined, in this section, by the following expression,

$$C_Y^B = \frac{\rho S_b(R^2\omega^2)R^2}{2EI}. \quad (17)$$

Taking this number into account, the elasticity equation (16) can be written in its dimensionless form as follows,

$$\frac{1}{C_Y^B}\frac{\partial^3\theta}{\partial s^3} = \frac{AU_p^2}{S_b}C_D\cos(\beta), \quad (18)$$

where S_b is the bending area of the blade (the planar surface of the blade) and $U_p^2 = (U_i/R\omega)^2 = 1 + 1/\lambda^2$. Note that in transitioning from Eq. (16) to Eq. (18), the curvilinear abscissa has been converted from a dimensional variable to its dimensionless counterpart s/R (referred to as s for convenience). The simplified model, which yields Equation (18), indicates that at any specific blade position, the deflection angle

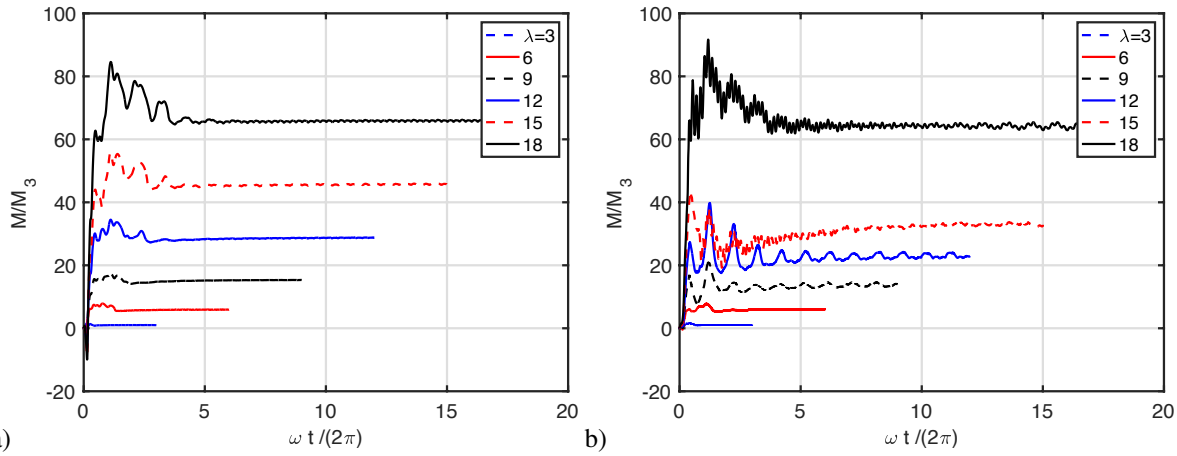

Fig. 20 Time evolution of the $z-$moment, M, for different tip speed ratios for a) the rigid case and b) the flexible case. The moment is made nondimensional using its value at $\lambda = 3$, denoted M_3. (For color, the reader is referred to the web version of this article).

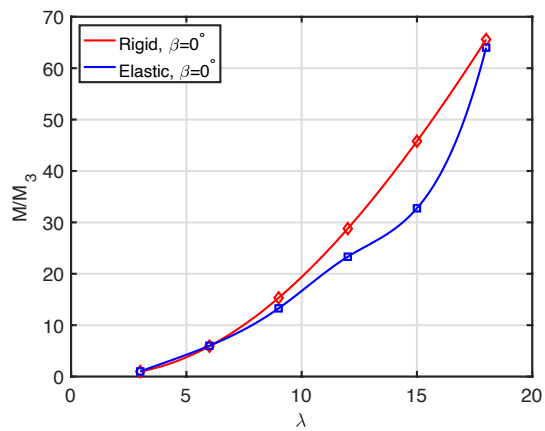

Fig. 21 Evolution of the $z-$moment, M, as a function of the tip speed ratio ($U = 0.18m/s$ and $\beta = 0°$). The moment is made nondimensional using its value at $\lambda = 3$, denoted M_3. (For color, the reader is referred to the web version of this article).

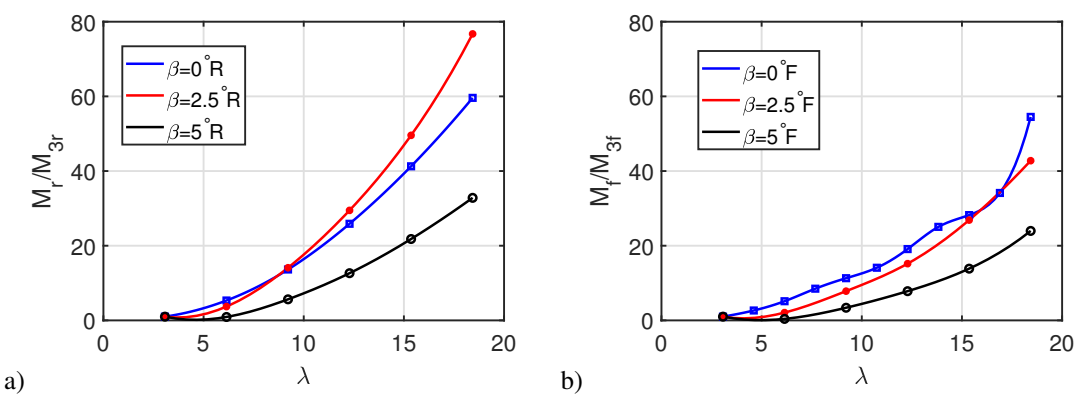

Fig. 22 Evolution of the $z-$moment, M, is depicted as a function of tip speed ratio, considering various pitch angles, β, in both (a) the rigid case and (b) the flexible case. The moment is made nondimensional using its value at $\lambda = 3$, denoted M_3. (For color, the reader is referred to the web version of this article).

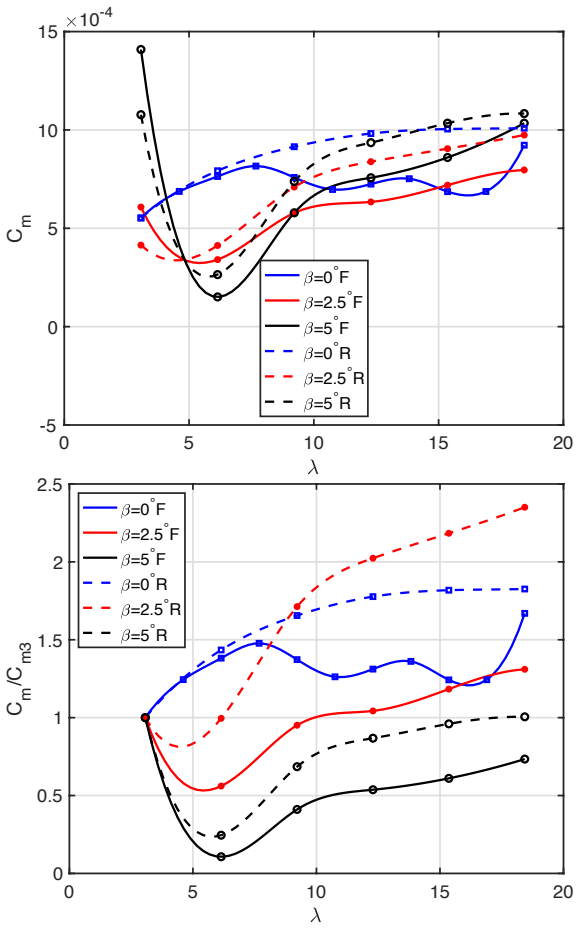

Fig. 23 Top: evolution of the $z-$moment coefficient, c_m, as a function of the tip speed ratio for different pitch angles, for the rigid case (R) and the flexible case (F). Bottom: the same, but C_m is devided by its value at $\lambda = 3$, C_{m3}. (For color, the reader is referred to the web version of this article).

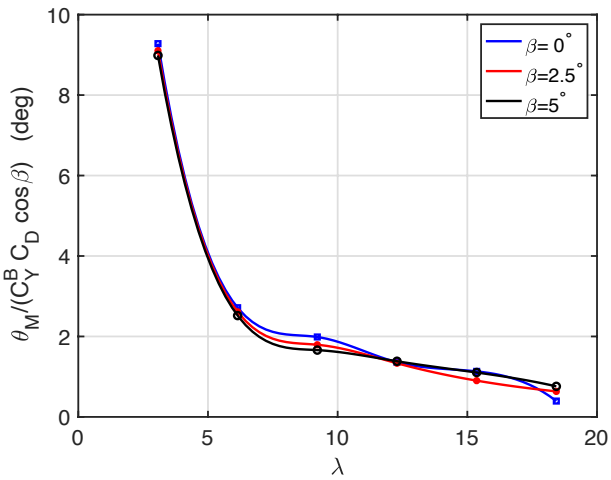

Fig. 24 The bending angle at the tip, denoted as θ_M and normalized by the drag coefficient C_D and the Cauchy number C_Y^B, is plotted as a function of the tip speed ratio for all flexible blades examined, with a speed of $0.18m/s$ ($U = 0.18m/s$). (For color, the reader is referred to the web version of this article).

divided by $C_Y^B C_D \cos(\beta)$ should solely depend on the tip speed ratio, denoted as λ. This assertion is substantiated through numerical simulations employing the complete model under investigation herein (Navier-Stokes equations, for the fluid flow, coupled with the linear elastic equations, for the solid motion). This phenomenon is depicted in Figure 24, wherein all deflection curves, corresponding to various pitches, converge when scaled by $\theta_M/(C_Y^B C_D \cos(\beta))$.

5 Conclusions

In this study, we conducted a numerical investigation into the fluid-structure interaction of a flexible rotor immersed in a turbulent water flow. Our objective was to gain insights into how flexibility influences the aerodynamic performance of rotors with flexible blades. Traditionally, rotor performance is primarily controlled by blade geometry and aerodynamic flow parameters. However, when flexibility is introduced, the original blade geometry is no longer maintained due to the deformations experienced during operation. Furthermore, the flow structure is altered by turbulence and blade vibrations, in contrast to rigid rotor configurations. Our prior study [27] aimed to comprehend and characterize these deformations in relation to elasticity and flow parameters. Our findings, here, reveal that flexibility exerts a substantial influence on rotor performance. Specifically, in the non-rotating case, the flexibility effect results in a reduction of the drag force. By allowing blade bending, the cross-sectional area exposed to the flow is diminished, thereby decreasing drag. We also examined how the aerodynamic performance of the rotor blade is affected by variations in the tip speed ratio, either amplifying or reducing it. Additionally, we discovered a scaling law governing the tip deformation angle when utilizing a modified Cauchy number. Furthermore, blade torsion contributes to rotor lift and torque, although further investigation is needed to fully understand its effect. Twisting is also a blade deformation, and any deformation induces a change in flow, which leads to a change in pressure and friction, consequently affecting lift and drag. Through this research, we have advanced our understanding of the interplay between rotor flexibility, deformation, and performance, contributing to the optimization of

rotor design and operational efficiency. However, further investigation is needed to elucidate the connection between elasticity, induced torsion, and the performance of rotors featuring flexible blades. Overall, our study highlights the importance of considering flexibility in rotor design and provides valuable insights into the complex fluid-structure interaction of flexible rotors in turbulent flow environments.

References

[1] S. Rehman, M. Mahbub Alam, L. Alhems, M. Mujahid Rafique, Horizontal axis wind turbine blade design methodologies for efficiency enhancement—a review. Energies **11**(3), 506 (2018)

[2] M.R. Abid, M.I. Sarwar, A.T.S.M. Shah, M. Shehryar, Gas turbine blade flow analysis comparison using cfd and wind tunnel. 9th International Bhurban Conference on Applied Sciences I& Technology (IBCAST) p. 203–207 (2012)

[3] P. Sakthivel, G. Rajamani, Design and analysis of modified wind turbine blades. Asian Journal of Research in Social Sciences and Humanities **7**(1), 166–177 (2017)

[4] E. Balla, J. Vad, A semi-empirical model for predicting the frequency of profile vortex shedding relevant to low-speed axial fan blade sections. 13th European Conference on Turbomachinery Fluid dynamics I& Thermodynamics

[5] J.F. Manwell, J.G. McGowan, A.L. Rogers, Wind energy explained: theory, design and application (John Wiley & Sons, 2010)

[6] M. Hussain, Y. Abdel-Nasser, A. Banawan, Y.M. Ahmed, Effect of hydrodynamic twisting moment on design and selection of flexible composite marine propellers. Ocean Engineering **220**, 108,399 (2021). https://doi.org/https://doi.org/10.1016/j.oceaneng.2020.108399

[7] Y. Young, Fluid–structure interaction analysis of flexible composite marine propellers. Journal of Fluids and Structures **24**(6), 799–818 (2008). https://doi.org/https://doi.org/10.1016/j.jfluidstructs.2007.12.010

[8] P. Lv, S. Prothin, F. Mohd-Zawawi, E. Benard, J. Morlier, J.M. Moschetta, Performance improvement of small-scale rotors by passive blade twist control. Journal of Fluids and Structures **55**, 25–41 (2015). https://doi.org/https://doi.org/10.1016/j.jfluidstructs.2015.01.008

[9] D.Q. Nguyen, G. Loianno, V.A. Ho, in 2020 3rd IEEE International Conference on Soft Robotics (RoboSoft) (2020), pp. 464–469. https://doi.org/10.1109/RoboSoft48309.2020.9115983

[10] J. Sicard, J. Sirohi, Aeroelastic stability of a flexible ribbon rotor blade. Journal of Fluids and Structures **67**, 106–123 (2016). https://doi.org/https://doi.org/10.1016/j.jfluidstructs.2016.09.010

[11] F. Gosselin, E. de Langre, B.A. Machado-Almeida, Drag reduction of flexible plates by reconfiguration. Journal of Fluid Mechanics **650**, 319–341 (2010). https://doi.org/10.1017/S0022112009993673

[12] S. Ramananarivo, R. Godoy-Diana, B. Thiria, Rather than resonance, flapping wing flyers may play on aerodynamics to improve performance. Proceedings of the National Academy of Sciences **108**(15), 5964–5969 (2011). https://doi.org/10.1073/pnas.1017910108. URL https://doi.org/10.1073%2Fpnas.1017910108

[13] L. Wang, X. Liu, A. Kolios, State of the art in the aeroelasticity of wind turbine blades: Aeroelastic modelling. Renewable and Sustainable Energy Reviews **64**(C), 195–210 (2016). https://doi.org/10.1016/j.rser.2016.06.00

[14] E. de Langre, Effects of wind on plants. Annual Review of Fluid Mechanics **40**(1), 141–168 (2008). https://doi.org/10.1146/annurev.fluid.40.111406.102135

[15] F.P. Gosselin, E. de Langre, Drag reduction by reconfiguration of a poroelastic system. Journal of Fluids and Structures **27**(7), 1111–1123 (2011). https://doi.org/https://doi.org/10.1016/j.jfluidstructs.2011.05.007

[16] L. Schouveiler, A. Boudaoud, The rolling up of sheets in a steady flow. Journal of Fluid Mechanics **563**, 71–80 (2006). https://doi.org/10.1017/

S0022112006000851

[17] H. Dai, H. Luo, J.F. Doyle, Dynamic pitching of an elastic rectangular wing in hovering motion. Journal of Fluid Mechanics **693**, 473 – 499 (2012)

[18] T. Bano, F. Hegner, M. Heinrich, R. Schwarze, Investigation of fluid-structure interaction induced bending for elastic flaps in a cross flow. Applied Sciences **10**(18) (2020)

[19] M. Motley, Z. Liu, Y. Young, Utilizing fluid–structure interactions to improve energy efficiency of composite marine propellers in spatially varying wake. Composite Structures **90**(3), 304–313 (2009). https://doi.org/https://doi.org/10.1016/j.compstruct.2009.03.011

[20] V. Cognet, S. Courrech du Pont, I. Dobrev, F. Massouh, B. Thiria, Bioinspired turbine blades offer new perspectives for wind energy. Royal Society **473**(2198) (2017). https://doi.org/https://doi.org/10.1098/rspa.2016.0726

[21] V. Cognet, S. Courrech du Pont, B. Thiria, Material optimization of flexible blades for wind turbines. Renewable Energy **160**, 1373–1384 (2020). https://doi.org/https://doi.org/10.1016/j.renene.2020.05.188

[22] A.D. Castillo, J.C. Jauregui-Correa, F. Herbert, K. K. Castillo-Villar, J.A. Franco, Q. Hernandez-Escobedo, A.J. Perea-Moreno, A. Alcayde, The effect of a flexible blade for load alleviation in wind turbines. Energies **14**(16) (2021)

[23] A.S. Eldemerdash, T. Leweke, Fluid–structure interaction of a flexible rotor in water. Journal of Fluids and Structures **103**, 103,259 (2021). https://doi.org/doi:10.1016/j.jfluidstructs.2021.103259

[24] S. Hoerner, S. Abbaszadeh, T. Maître, O. Cleynen, D. Thévenin, Characteristics of the fluid–structure interaction within darrieus water turbines with highly flexible blades. Journal of Fluids and Structures **88**, 13–30 (2019). https://doi.org/https://doi.org/10.1016/j.jfluidstructs.2019.04.011

[25] Q. Gao, S. Lian, H. Yan, Aerodynamic performance analysis of adaptive drag-lift hybrid type vertical axis wind turbine. Energies **15**(15) (2022)

[26] K. Oukassou, S.E. Mouhsine, A.E. Hajjaji, B. Kharbouch, Comparison of the power, lift and drag coefficients of wind turbine blade from aerodynamics characteristics of naca0012 and naca2412. Procedia Manufacturing **32**, 983–990 (2019)

[27] M. Fakhfekh, W. Ben Amira, M. Abid, A. Maalej, Numerical simulations of the wake and deformations of a flexible rotor blade in a turbulent flow. Physics of Fluids **35**(5) (2023). https://doi.org/10.1063/5.0147021

[28] Y. Bazilevs, M.C. Hsu1, J. Kiendl, R. Wüchner, K.U. Bletzinger, 3d simulation of wind turbine rotors at full scale. part ii:fluid–structure interaction modeling with composite blades. International Journal for Numerical Methods in Fluid **65**(1-3), 236–253 (2011). https://doi.org/10.1002/fld.2454

[29] T. Richter, Fluid-structure interactions: models, analysis and finite elements, vol. 118 (Springer, 2017)

[30] M.B. Ageze, Y. Hu, H. Wu, Comparative study on uni- and bi-directional fluid structure coupling of wind turbine blades. Energies **10**(10) (2017)

[31] S. Tatum, C. Frost, M. Allmark, D. O'Doherty, A. Mason-Jones, P. Prickett, R. Grosvenor, C. Byrne, T. O'Doherty, Wave–current interaction effects on tidal stream turbine performance and loading characteristics. International Journal of Marine Energy **14**, 161–179 (2016). https://doi.org/https://doi.org/10.1016/j.ijome.2015.09.002

[32] M. Badshah, S. Badshah, J. VanZwieten, S. Jan, M. Amir, S.A. Malik, Coupled fluid-structure interaction modelling of loads variation and fatigue life of a full-scale tidal turbine under the effect of velocity profile. Energies **12**(11) (2019). https://doi.org/10.3390/en12112217

[33] T. Aurégan, B. Thiria, S. Courrech du Pont, Scaling the thrust and deformations of a rotor with flexible blades. Phys. Rev. Fluids **8**, 044,401 (2023). https://doi.org/10.1103/PhysRevFluids.8.044401. URL https://link.aps.org/doi/10.1103/PhysRevFluids.8.044401

[34] A.L. Prasuhn, Fundamentals of Fluid Mechanics (Prentice Hall, Englewood Cliffs, New Jersey, 1980)

[35] F. GOSSELIN, E. de LANGRE, B.A. MACHADO-ALMEIDA, Drag reduction of flexible plates by reconfiguration. Journal of Fluid Mechanics **650**, 319–341 (2010). https://doi.org/10.1017/S0022112009993673